Karlsruhe Institute of Technology
Faculty of Chemistry and Biosciences
Institute for Chemical Technology and Polymer Chemistry

Numerical simulation of the electrochemical behavior of a LSM-YSZ composite cathode in a Solid Oxide Fuel Cell (SOFC) using a reduced kinetic model

Bachelor thesis
By Aaron Useche Esclasans
Group of Prof. Dr. Olaf Deutschmann

Supervisors:
Prof. Dr. Olaf Deutschmann
Aayan Banerjee

20.06.2017 – 20.10.2017

Abstract

A reduced kinetic model is used to simulate the electrochemical impedance spectra (EIS) and steady state polarization curves of the oxygen reduction reaction (ORR) measured on LSM-YSZ composite cathodes sintered on dense YSZ electrolytes with different microstructures and under multiple conditions. The model assumes the dissociation of a superoxo-like ad-atom O^{-}_{2,LSM_s} on the LSM surface to be the rate determinant step (RDS) with all other steps of the mechanism being fast and in equilibrium. The mechanism is based on the work of A. Banerjee and O. Deutschmann [1] and is part of a multi-physics based transient, continuum model which simulates a button half-cell. The proposed model is first fitted to experimental EIS measurements to obtain a realistic set of kinetic and thermodynamic parameters. The model was then validated by simulating experimental data sets from other sources without reparametrizing the kinetics and the thermodynamics. The proposed model can simulate the experimental data with a certain degree of discrepancy. However, the large discrepancies, obtained by simulating at temperatures outside the original temperature range in which the model was calibrated are strong indicators that the model is not fully intrinsic. Moreover, the lack of microstructural information from the simulated cells increases the number of parameters that must be estimated, which also increases the uncertainty of the model.

List of abbreviations

Abbreviation	Meaning	Unit
E_a	Activation energy	$J\ mol^{-1}$
c_i	Activity of participating species i	
k_b	Backward reaction rate constant	
R_p	Cathode polarization resistance	$\Omega\ cm^2$
E_{cell}	Cell voltage	V
CT	Charge transfer reaction	
α	Charge transfer symmetry factor	
DETCHEM	Detailed Chemistry	
DL	Double layer	
EIS	Electrochemical impedance spectroscopy	
R	Gas constant	$bar\ m^3\ K^{-1}\ mol^{-1}$
ΔG	Gibbs free energy change	$J\ mol^{-1}$
$\dot{s}_k$	Heterogeneous molar production of k	$mol\ m\ s^{-1}$
$C_{DL}^{LSM/YSZ}$	Interfacial DL capacitance	$F\ cm^{-2}$
LSM	Lanthanum strontium manganite	
X_k	Mole fraction of k	
OCV	Open circuit voltage	
ORR	Oxygen reduction reaction	
d_p	Particle diameter	m
d_{pore}	Pore diameter	m
ϵ	Porosity	
E_{CT}	Potential difference between the phases participating in a CT reaction	V
k^0	Pre-exponential factor of the reaction rate constant	
A_2	Pre-exponential fitting parameter	
RDS	Rate determining step	
r	Reaction rate	$mol\ s^{-1}$
k	Reaction rate constant	
SOFC	Solid oxide fuel cell	
$A_{gas/LSM}^V$	Specific area of the LSM surface exposed to the gas phase	m^{-1}
$A_{LSM,YSZ}^V$	Specific surface area available at the LSM-YSZ bulk interface	m^{-1}
λ_{3PB}^V	Specific three phase boundary length	m^{-2}
$\nu_{k,j}$	Stoichiometric coefficient of species k in reaction j	
θ	Surface coverage fraction	
T	Temperature	K
k^t	Thermal component of the rate constant	
3PB	Three-phase boundary	
τ	Tortuosity	
Γ_s	Total available surface density for adsorption site-type s	
$\upsilon_{f,LSM}$	Volume fraction of the LSM bulk phase	
$\upsilon_{f,YSZ}$	Volume fraction of the YSZ bulk phase	
YSZ	Yttria-stabilized zirconia	

Table of contents

1. Introduction

The climate change and the need for new power generation technologies have driven Solid Oxide Fuel Cells (SOFCs) further into the focus of research in the last decades as an efficient, environmentally friendly, and fuel-versatile source of electric power [2]. “Due to its high operating temperature, the SOFC offers several potential advantages over polymer-based fuel cells” [2]. One of those advantages is the ability to reform hydrocarbons so that they can be used directly as fuels [2], therefore expanding the applicability of fuel cells to other fuels apart from hydrogen H_2. The basic working principle of a SOFC is illustrated in Figure 1.

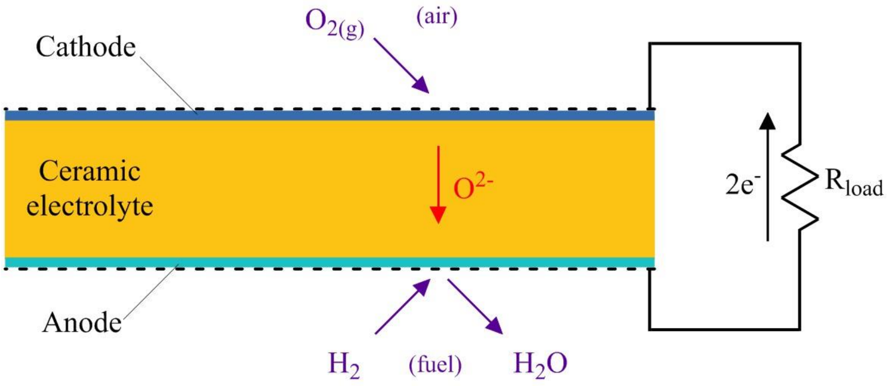

Figure 1. Schematic representation of the working principle of a SOFC. Adapted from S.B. Adler [2].

The cathode side of the cell is usually supplied with air containing oxygen O_2. The Oxygen is reduced at the cathode following the overall Oxygen Reduction Reaction (ORR) [2]:

$$2e^- + \frac{1}{2}O_2 \rightarrow O^{2-} \tag{1}$$

The so formed oxygen ions O^{2-} migrate through the solid ceramic electrolyte until they reach the anode. There they undergo the opposite half-cell reaction by oxidizing the fuel to produce water H_2O and carbon dioxide CO_2 [2]. The electrons, which are liberated at the anode, cannot trespass electrolyte, since it is commonly made of electric insulating materials. Therefore, they are transported over an external circuit, where they perform work, to the cathode where they are consumed in the oxidation reaction [2].

A ceramic material commonly used as an electrolyte is yttria-stabilized zirconia (YSZ), with common doping levels of 8% yttria [1]. For the cathode “acceptor-doped transition metal oxides with high electron conductivities serve as attractive low-cost alternatives to noble metals". [1] A good example is lanthanum strontium manganite (LSM), which is a good electron conductor and readily catalyzes the ORR [1].

Even though LSM/YSZ SOFCs have been intensively investigated for the last 45 years several factors still limit their commercial application [2]. "In fact, cathodic polarization due to slow ORR kinetics is widely acknowledged to be the dominant source of losses" [1]. It is therefore not surprising that over the last two decades great efforts have been made to understand the underlying mechanism in order to be able to develop more efficient electrode materials and structures [2]. An example of such an effort is the work published by A. Banerjee and O. Deutschmann [1] where a multi-physics based transient, continuum model was developed to investigate the ORR kinetics. "The model coupled species, electron and ion transport through the porous cathode to surface and electro-chemistry" [1]. The ORR itself was modeled using a series of the elementary steps. Elementary-kinetic models have several advantages over global kinetic ones (e.g. the Butler-Volmer approach). The first is that no a priori assumptions over the rate limiting step of the mechanism are done. The second is that it allows to simulate under transient conditions, i.e. under non-equilibrium conditions, which is for instance always the case when the anode is operated under internal-reforming conditions [3]. By comparing their simulations to experimental data [4–6] Banerjee and Deutschmann were able to propose and support a mechanism for the ORR in a LSM-YSZ composite cathodes sintered on dense YSZ electrolytes. By means of a sensitivity analysis they also identified different rate determining steps (RDS) at different polarizations [1].

Using elementary kinetics poses however several challenges. Each reaction involves a series of kinetic parameters (pre-exponential factor and activation energy) as well as thermodynamic properties (enthalpies and entropies) for all participating species for which thermodynamically consistent values have to be found [1]. In case of species or reactions for which data is not available the required parameters must be fitted to experimental data, increasing the uncertainty of the model [1]. The objective of this work is to reduce the elementary kinetic model proposed by Banerjee and Deutschmann to a model with only one RDS, therefore reducing the number of fitting parameters. The so obtained model is first fitted to the same data set from A. Barbucci et al. [4] as the original model and then validated against measurements done on other LSM-YSZ composite cathodes with different microstructural characteristics (e.g. cathode thickness and porosity) [5,7–11]. The idea is to obtain an intrinsic model, which can reproduce large sets of experimental data from distinct and independent sources for the ORR on LSM-YSZ composite cathodes sintered on dense YSZ electrolytes [1].

2. Methodology

A. Banerjee and O. Deutschmann [1] proposed three different mechanisms for the ORR from which one yielded the best results [4,5,7]. The mechanism involved a parallel surface and bulk path. By means of a sensitivity analysis of the most successful mechanism, the dependency of the cathode polarization resistance $\mathrm{R_p}$ on the kinetic and charge transport parameters was investigated. Banerjee and Deutschmann concluded that the bulk phase path had a negligible contribution on the $\mathrm{R_p}$, regardless of the oxygen partial pressure, temperature, or polarization. This analysis also revealed, in agreement to the knowledge on LSM-YSZ cathodes [2], that the RDS changes from the dissociation of a superoxo-like ad-atom $\mathrm{O^-_{2,LSM_s}}$ on the LSM surface at zero polarization, i.e. at open circuit voltage (OCV), to a co-limitation with the spillover of $\mathrm{O^-_{LSM_{3PB}}}$ oxygen ions across the three phase boundary (3PB) between the LSM and the YSZ. This rate limitation through a surface charge transfer (CT) reaction was also reflected in a high dependency on the specific area of the LSM surface exposed to the gas phase $\mathrm{A^V_{gas/LSM}}$. Finally, the $\mathrm{R_p}$ was also found to be particularly sensitive to the ionic transport through the YSZ phase in the cathode.

This work makes use of the most successful mechanism proposed from Banerjee and Deutschmann by ignoring the bulk path and assuming the dissociation of a superoxo-like ad-atom $\mathrm{O^-_{2,LSM_s}}$ on the LSM surface to be the RDS while all others are fast and in equilibrium (a detailed description of the kinetic model used in this work can be found in section 2.4). The proposed model is first fitted to experimental electrochemical impedance spectroscopy (EIS) data at OCV from A. Barbucci et al. [4] in order to find the best values for the kinetic parameters (i.e. the pre-exponential factor and the activation energy). The model is then used to simulate the experimental EIS curves at OCV from J.S. Cronin et al. [5] and J. Nielsen and J. Hjelm [7] and the experimental steady state polarization curves from A. Barbucci et al. [4], A.C. Co et al. [8], J. Soderberg et al. [9], Y.J. Leng et al. [11], and K. Hayashi et al. [10] without reparametrizing the kinetics and the thermodynamics.

The experimental data sets used here are chosen because a good amount of information regarding the microstructure of the tested cathode and electrolyte is provided. Without this information, it is impossible to prove that the model is intrinsic. Finally, the simulation of polarization curves is of interest for this work, as an operating cell, i.e. a cell which produces electrical current, is always under polarization. A kinetic model in which the spillover of oxygen ions across the three-phase boundary is co-limiting was not considered in this work, on one hand due to time constrains, on the other because no experimental EIS data performed on LSM-YSZ composite cathodes under polarization was available.

2.1. Description of the model

The computational model presented in this work is part of the computational package DETCHEM (Detailed Chemistry) which was originally published by H. Zhu et al. [12] and V.M. Janardhanan and O. Deutschmann [13]. Most of the specific calculations and conditions to be applied in the model are taken from A. Banerjee and O. Deutschmann [1]. Any changes done to the computational model during this work are specifically pointed out and described.

The model simulates a button half-cell. The half-cell consists of a porous composite cathode of lanthanum strontium manganite (LSM) and yttria-stabilized zirconia (YSZ) on a dense YSZ electrolyte [1] (see Figure 2). The path of the oxygen molecules is simulated from the moment they enter the porous composite cathode from the bulk stream [1]. Ordinary and Knudsen diffusion along with bulk (Darcy) flow describe the distribution of oxygen through the porous structure of the cathode. Gas-phase oxygen O_2 is chemisorbed on the LSM surface and spills over to the YSZ surface as O_2^{2-} ions. The O_2^{2-} oxygen ions are incorporated into the YSZ bulk phase and transported to the electrolyte [1]. A detailed description of the media transport and the electrochemistry can be found in sections 2.2 – 2.4.

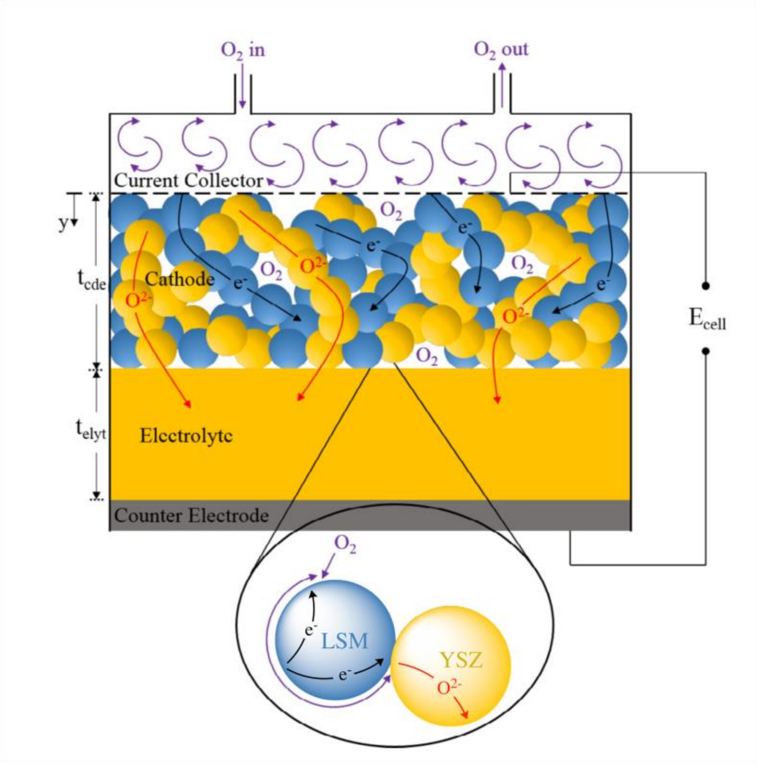

Figure 2. Schematic representation of the modeling domain illustrating the various transport phenomena and oxygen reaction pathways through the LSM and YSZ particles. Adapted from A. Banerjee and O. Deutschmann [1].

“Several assumptions are made in the model” [1]:

1. “The cathode is approximated as a homogeneous continuum of spherical particles with random percolating clusters” [1].
2. “The modeling domain is isothermal” [1].
3. “The species and charge transport are modeled in one dimension (1D-model) along the thickness of the cell” [1].
4. “The current collector mesh has no impact on the gas transport at the bulk stream-cathode interphase” [1].
5. “The current collector is assumed to be a pure electronic conductor and the dense electrolyte is assumed to be a pure ionic conductor” [1].
6. “The LSM bulk phase is also assumed to be a pure electronic conductor. The transport of oxygen ions trough the LSM bulk phase is assumed to be negligible”.
7. “The principle of electroneutrality holds in the cathode” [1].
8. “All electronic transport in the LSM bulk phase and all ionic transport in the YSZ bulk phase are due to electrostatic migration only” [1].

9. “The cell voltage E_{cell} is equal to the sum of the potential drops across the cathode and the electrolyte” [1].
10. The ORR is modeled using a reduced kinetic mechanism (see section 2.4).
11. “Reactions occur neither at the current collector on the cathode nor at the cathode-electrolyte interfaces” [1].
12. “Direct oxygen adsorption on YSZ is not considered” [1].

2.2. Porous media transport

All transport phenomena are represented by the model in one dimension (1-D model) along the button cell thickness y [1]. The equations for the porous media transport are contained in the DETCHEM program package and were not modified in any way during this work. All governing equations are taken from A. Banerjee and O. Deutschmann [1], unless otherwise stated, and are summarized in Table 1. A detailed description of this equations as well as the parameters involved can be found in A. Banerjee and O. Deutschmann [1] and are not repeated here.

Table 1. Summary of the governing equations describing the porous media transport in the model. Adapted from A. Banerjee and O. Deutschmann [1].

Description	Model equation	Variables	Equation N°	Reference
Density of the gas-phase species k	$\frac{\partial(\epsilon\rho_k)}{\partial t} = -\frac{\partial(J_k W_k)}{\partial y} + \dot{s}_k W_k A^V_{gas/LSM}$	$k = 1, \dots, K_g$ ϵ: Porosity of the porous media J_k: Molar flux of k W_k: Molecular weight of k $\dot{s}_k$: Heterogeneous molar production of k	(2)	[1]
Total density of the fluid	$\frac{\partial(\epsilon\rho)}{\partial t} = -\sum_{k=1}^{K_g} \frac{\partial(J_k W_k)}{\partial y} + \sum_{k=1}^{K_g} \dot{s}_k W_k A^V_{gas/LSM}$	$A^V_{gas/LSM}$: Specific area of the LSM surface exposed to the gas phase K_g: Total number of gas-phase species	(3)	[1]
Species molar flux (Dusty-Gas model)	$J_k = -\left[\sum_{l=1}^{K_g} D^{DGM}_{kl} \nabla[X_l] + \left(\sum_{l=1}^{K_g} \frac{D^{DGM}_{kl}[X_l]}{D^e_{l,Kn}}\right) \frac{B_g}{\mu} \nabla p\right]$	∇p: Pressure gradient μ: Mixture viscosity	(4)	[1]
Permeability	$B_g = \frac{\epsilon^3 d_p^2}{72\tau(1-\epsilon)^2}$	d_p: Particle diameter τ: Porous media tortuosity	(5)	[15]
Matrix of diffusion coefficients	$D^{DGM}_{kl} = H^{-1}$		(6)	[1]
Elements of the H matrix	$h_{kl} = \left[\frac{1}{D^e_{k,Kn}} + \sum_{j \neq k} \frac{X_j}{D^e_{kj}}\right] \delta_{kl} + (\delta_{kl} - 1) \frac{X_k}{D^e_{kl}}$	X_k: Mole fraction of k δ_{kl}: Kronecker delta	(7)	[1]
Effective Knudsen diffusion coefficient	$D^e_{k,Kn} = \frac{\epsilon}{\tau} \frac{d_{pore}}{3} \sqrt{\frac{8RT}{\pi W_k}}$	d_{pore}: Pore diameter	(8)	[1]
Effective binary diffusivity between species k and l	$D^e_{kl} = \frac{\epsilon}{\tau} D_{kl}$	D_{kl}: Binary diffusivities	(9)	[1]

Description	Model equation	Variables	Equation N°	Reference
Mass fraction of k at the bulk stream-cathode interface	$Y_{k,gas/cde} = \frac{\dot{m}_{in}Y_{k,in} - J_{k,gas/cde}W_k}{\dot{m}_{in} - \sum_{k=1}^{Kg} J_{k,gas/cde}W_k}$	$Y_{k,in}$: Mass fraction of k at the bulk stream inlet $\dot{m}_{in}$: Mass flow rate of gas at the bulk stream inlet $J_{k,gas/cde}$: Molar flux of k at the bulk stream-cathode interface	(10)	[1]
Surface coverage of a reaction intermediate k	$\frac{\partial \theta_k}{\partial t} = \frac{\dot{s}_k}{\Gamma_s}$	Γ_s: Density of available sites on the surface (surface densiuty)	(11)	[1]
Relation of the local bulk phase potential to current density in each phase	$\frac{\partial}{\partial y}\left(\sigma_{el,LSM}^{e} \frac{\partial \phi_{LSM_b}}{\partial y}\right) = i_F^V + i_{DL}^V$	ϕ_{LSM_b}: Potential of the LSM bulk phase	(12)	[16]
	$\frac{\partial}{\partial y}\left(\sigma_{io,YSZ}^{e} \frac{\partial \phi_{YSZ_b}}{\partial y}\right) = -\left(i_F^V + i_{DL}^V\right)$	ϕ_{YSZ_b}: Potential of the YSZ bulk phase	(13)	[16]
Faradaic current density	$i_F^V = -2F\left(A_{LSM,YSZ}^V r_{2PB} + \lambda_{3PB}^V r_{3PB}\right)$	$A_{LSM,YSZ}^V$: Specific surface area available at the LSM-YSZ bulk interface λ_{3PB}^V: Specific three phase boundary length r_{2PB}: Charge transfer reaction rate at the two-phase boundary r_{3PB}: Charge transfer reaction rate at the three-phase boundary	(14)	[1]
Capacitive current density	$i_{DL}^V = A_{LSM/YSZ}^V \frac{\partial}{\partial t}\left(C_{DL}^{LSM/YSZ} \Delta\phi\right)$	$C_{DL}^{LSM/YSZ}$: Interfacial DL capacitance $\Delta\phi$: Difference between the LSM and YSZ bulk phase potentials at the interface	(15)	[1]
Effective electronic conductivity of the LSM bulk phase	$\sigma_{el,LSM}^{e} = \sigma_{el,LSM}\left[(1-\epsilon)\upsilon_{f,LSM}\gamma_{LSM}\right]^{1.5}$	$\upsilon_{f,LSM}$: Volume fraction of the LSM bulk phase γ_{LSM}: Percolation probability of the LSM phase	(16)	[17]

Description	Model equation	Variables	Equation N°	Reference
Effective ionic conductivity of the YSZ bulk phase	$\sigma^{e}_{io,YSZ} = \sigma_{io,YSZ}\left[(1-\epsilon)\upsilon_{f,YSZ}\gamma_{YSZ}\right]^{1.5}$	$\upsilon_{f,YSZ}$: Volume fraction of the YSZ bulk phase γ_{YSZ}: Percolation probability of the YSZ phase	(17)	[17]
Electronic conductivity of the LSM bulk phase	$\sigma_{el,LSM} = (8.855 \times 10^{5}/T) \cdot \exp(-1082.5/T)\mathrm{Scm}^{-1}$		(18)	[18]
Ionic conductivity of the YSZ bulk phase	$\sigma_{io,YSZ} = 3.34 \times 10^{2} \cdot \exp(-10300/T)\mathrm{Scm}^{-1}$		(19)	[19]
Percolation probability of phase m	$\gamma_{m} = 1 - \left(\frac{4.236 - Z_{m,m}}{2.472}\right)^{3.7}$	$Z_{m,m}$: Number of contact sites between particles of phase m	(20)	[20]

2.3. Electrochemistry

The rate of an elementary step r_p is given by the law of mass action, [1]

$$r_p = \left(k_{f,p} \prod_{i \in R_{f,p}} c_i^{\nu'_i} - k_{b,p} \prod_{i \in R_{b,p}} c_i^{\nu''_i} \right) \tag{21}$$

where "ν'_i and ν''_i are stoichiometric coefficients of each reactant in the forward and in the backward reaction respectively. $k_{f,p}$ and $k_{b,p}$ are the forward and backward reaction rate coefficients. c_i is the activity of the participating species I" [1]. The activity of a gas-phase species i is its molar fraction $X_{i,g}$ [21]. The activity of a species i adsorbed on a surface s is its surface coverage $\Gamma_s\theta_{i,s}$, where Γ_s is the total available surface density for the adsorption site-type s and $\theta_{i,s}$ is the fraction of sites occupied by species i [21]. The activity of a bulk lattice species is its mole fraction in the bulk phase. $R_{f,p}$ and $R_{b,p}$ represent all reactants in the forward reaction and in the backward reaction respectively [1].

The rate coefficient of a CT reaction can be expressed as the following [1]:

$$k = k^t \exp\left(-\frac{n\alpha F E_{CT}}{RT}\right) \tag{22}$$

Here "F and R are the Faraday and the gas constant respectively," [1] k^t is the thermal component of the rate constant, "n is the number of electrons/holes transferred, α is the charge transfer symmetry factor fixed to 0.5, E_{CT} is the potential difference between the phases participating in the CT reaction, and T is the temperature" [1]. The rate coefficient of a forward and a backward CT reaction in the cathode are written respectively as:

$$k_f = k_f^t \exp\left(-\frac{n\alpha_c F E_{CT}}{RT}\right) \tag{23}$$

$$k_b = k_b^t \exp\left(+\frac{n\alpha_a F E_{CT}}{RT}\right) \tag{24}$$

The thermal component of the rate constant of a forward reaction can be written in a modified Arrhenius form as [21]:

$$k_f^t = k_f^0 T^n \exp\left(-\frac{E_{a,f}}{RT}\right) \tag{25}$$

where "k_f^0 is the pre-exponential factor, $E_{a,f}$ is the thermal activation energy of the forward reaction and T^n is the temperature dependence of the rate constant" [21]. To ensure thermodynamic consistency the thermal component of the rate constant of the backward reaction is calculated from the reaction equilibrium constant K [21]:

$$K^t = \frac{k_f^t}{k_b^t} = \exp\left(-\frac{\Delta G_R}{RT}\right) \tag{26}$$

where ΔG_R is the Gibbs free energy change for the reaction. If all species in a reaction are at the same electric potential, that is $E_{CT} = 0$, the rate constant expression reduces to that of a thermal reaction [21]. Finally the molar production rate of species k due to both surface and CT reactions can be written as [1]:

$$\dot{s}_k = f \sum_j \nu_{k,j} r_j \tag{27}$$

Here "j represents a reaction in which k is involved, $\nu_{k,j}$ is the stoichiometric coefficient of k in that reaction, and f is a factor which has different values for different types of reactions (=1 for surface to bulk transfer reaction)" [1].

2.4. Derivation of the reduced kinetic equation

The elementary steps for the ORR are taken from A. Banerjee and O. Deutschmann [1] and are listed along with all relevant kinetic and thermodynamic parameters in Table 2.

Table 2. ORR Mechanism. Adapted from A. Banerjee and O. Deutschmann [1].

Reaction		k_f^0	$E_{a,f}$ (kj mol^{-1})	Reference
R1	$O_{2,g} + *_{LSM_s} \rightleftharpoons O^-_{2,LSM_s} + h^{\cdot}_{LSM_b}$			
R2	$O^-_{2,LSM_s} + *_{LSM_s} \rightleftharpoons 2O^-_{LSM_s} + h^{\cdot}_{LSM_b}$	Fit	190	[1]
R3	$O^-_{LSM_s} \rightleftharpoons O^-_{LSM_{3PB}}$			
R4	$O^-_{LSM_{3PB}} + *_{YSZ_s} \rightleftharpoons O^{2-}_{YSZ_s} + *_{LSM_s} + h^{\cdot}_{LSM_b}$			
R5	$O^{2-}_{YSZ_s} + V^{\cdot\cdot}_{O,YSZ_b} \rightleftharpoons O^{x}_{O,YSZ_b} + *_{YSZ_s} + h^{\cdot}_{LSM_b}$			

[a] Sticking coefficient.

Since step R2 is considered here to be the rate determining step (RDS) and all other steps are considered to be fast and in equilibrium only the activation energy for the forward reaction R2, $E_{a,f2}$, is relevant, as it will be shown in this section. The pre-exponential factor of the forward reaction R2, k_{f2}^0, is obtained by fitting along with other parameters. Step R1 represents the chemisorption of gas-phase oxygen $O_{2,g}$ on an adsorption site of the LSM surface $*_{LSM_s}$ by consuming one electron to form a superoxo-like ad-atom O^-_{2,LSM_s}.The superoxo-like ad-atom then dissociates in step R2 into two $O^-_{LSM_s}$ ad-atoms by consuming another electron. Step R3 represents the diffusion of the $O^-_{LSM_s}$ along the LSM surface to the three-phase boundary (3PB). The $O^-_{LSM_{3PB}}$ at the 3PB then spills over to the YSZ surface on to an adsorption site $*_{YSZ_s}$ and consumes one last electron to form a $O^{2-}_{YSZ_s}$ ion. This ion is finally incorporated into the YSZ bulk phase by filling a vacancy in the lattice $V^{\cdot\cdot}_{O,YSZ_b}$ to form a O^x_{O,YSZ_b}. $h^{\cdot}_{LSM_b}$ represents electron holes in the LSM bulk phase [1]. All steps of the mechanism are illustrated in Figure 3.

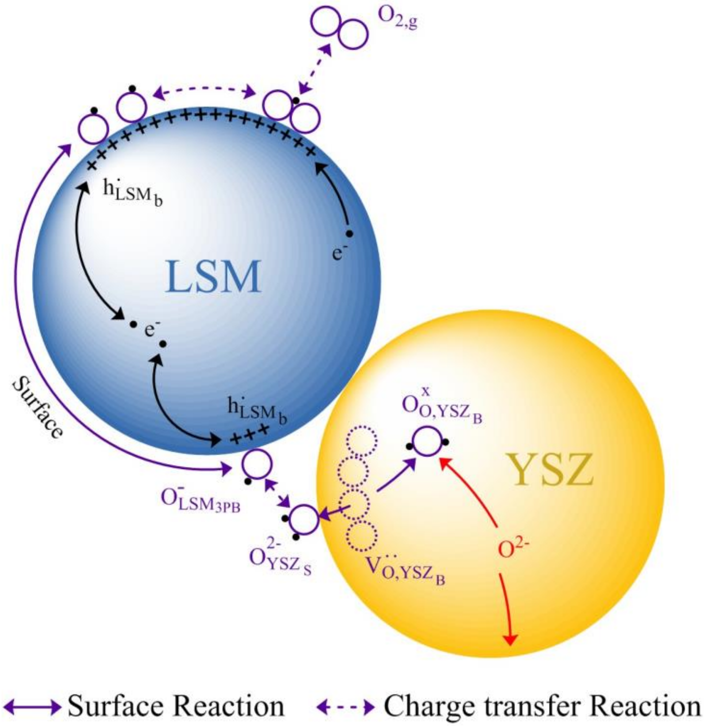

Figure 3. Schematic representation of the ORR mechanism used in the model. Adapted from A. Banerjee and O. Deutschmann [1].

For each step of the mechanism a kinetic rate equation can be written as the following:

$$r_1 = k^t_{f1} X_{O_{2,g}} \theta_{*LSM_s} \exp\left(\frac{-\alpha_{c1} F E_{LSM_{S/B}}}{RT}\right) - k^t_{b1} \theta_{O^-_{2,LSM_s}} \exp\left(\frac{\alpha_{a1} F E_{LSM_{S/B}}}{RT}\right) \tag{28}$$

$$r_2 = k^t_{f2} \theta_{O^-_{2,LSM_s}} \theta_{*LSM_s} \exp\left(\frac{-\alpha_{c2} F E_{LSM_{S/B}}}{RT}\right) - k^t_{b2} \theta^2_{O^-_{LSM_s}} \exp\left(\frac{\alpha_{a2} F E_{LSM_{S/B}}}{RT}\right) \tag{29}$$

$$r_3 = k_{f3} \theta_{O^-_{LSM_s}} - k_{b3} \theta_{O^-_{LSM_{3PB}}} \tag{30}$$

$$r_4 = k^t_{f4} \theta_{O^-_{LSM_{3PB}}} \theta_{*YSZ_s} \exp\left(\frac{-\alpha_{c4} F E_{3PB}}{RT}\right) - k^t_{b4} \theta_{O^{2-}_{YSZ_s}} \theta_{*LSM_s} \exp\left(\frac{\alpha_{a4} F E_{3PB}}{RT}\right) \tag{31}$$

$$r_5 = k_{f5} \theta_{O^{2-}_{YSZ_s}} X_{V^{\cdot\cdot}_{O,YSZ_b}} - k_{b5} \theta_{*YSZ_s} X_{O^x_{O,YSZ_b}} \tag{32}$$

Here $\mathrm{E_{LSM_{S/B}}}$ represents electric potential difference across the double layer (DL) between the LSM surface and the LSM bulk. The DL is formed due to the oxygen ions adsorbed on the LSM surface and the electron holes in the LSM bulk. $\mathrm{E_{3PB}}$ is the electric potential difference across the 3PB between the LSM and the YSZ surface. $\mathrm{X_{V_{O,YSZ_b}^{\cdot\cdot}}}$ and $\mathrm{X_{O_{O,YSZ_b}^{x}}}$ are the bulk mole fractions of the lattice species $\mathrm{V_{O,YSZ_b}^{\cdot\cdot}}$ and $\mathrm{O_{O,YSZ_b}^{x}}$ respectively, and are equal to 0.0374 and 0.9626 for an yttria doping level of %8 in Zirconia [22]. By assuming steps R1, R3, R4, and R5 to be in equilibrium ($\mathrm{r_1 = r_3 = r_4 = r_5 = 0}$) Eqs. 27, 29, 30, and 31 can be rewritten as:

$$\frac{\theta_{O_{2,LSM_s}^-}}{X_{2,g}\theta_{*LSM_s}} = K_1^t exp\left(\frac{-(\alpha_{c1}+\alpha_{a1})\mathrm{FE_{LSM_{S/B}}}}{\mathrm{RT}}\right) \tag{33}$$

$$\frac{\theta_{\mathrm{O^-_{LSM_{3PB}}}}}{\theta_{\mathrm{O^-_{LSM_s}}}} = \mathrm{K_3} \tag{34}$$

$$\frac{\theta_{\mathrm{O^{2-}_{YSZ_s}}}\theta_{\mathrm{*LSM_s}}}{\theta_{\mathrm{O^-_{LSM_{3PB}}}}\theta_{\mathrm{*YSZ_s}}} = \mathrm{K_4^t}\mathrm{exp}\left(\frac{-(\alpha_{c4}+\alpha_{a4})\mathrm{FE_{3PB}}}{\mathrm{RT}}\right) \tag{35}$$

$$\frac{\theta_{\mathrm{*YSZ_s}}\mathrm{X_{O_{O,YSZ_b}^{x}}}}{\theta_{\mathrm{O^{2-}_{YSZ_s}}}\mathrm{X_{V_{O,YSZ_b}^{\cdot\cdot}}}} = \mathrm{K_5} \tag{36}$$

By substituting Eqs. 32 – 35 in Eq. 28 the following expression for the rate of step R2 is obtained:

$$\begin{aligned}\mathrm{r_2} &= \mathrm{k_{f2}^t K_1^t X_{O_{2,g}}}\theta^2_{\mathrm{*LSM_s}}\mathrm{exp}\left(\frac{-(\alpha_{c2}+1)\mathrm{F}\Delta\phi}{\mathrm{RT}}\right)\\ &- \frac{\mathrm{k_{b2}^t}}{(\mathrm{K_3K_4^tK_5})^2}\theta^2_{\mathrm{*LSM_s}}\left(\frac{\mathrm{X_{O_{O,YSZ_b}^{x}}}}{\mathrm{X_{V_{O,YSZ_b}^{\cdot\cdot}}}}\right)^2\mathrm{exp}\left(\frac{(\alpha_{c2}+2)\mathrm{F}\Delta\phi}{\mathrm{RT}}\right)\end{aligned} \tag{37}$$

Here it is assumed that the electric potential differences for all CT reactions equal the electric potential drop of the half-cell $\Delta\phi$ (labeled as $\mathrm{E_{cell}}$ in Figure 2). That is the difference between the potential of the current collecting grid on top of the cathode (set to $\mathrm{E_{cell}}$) and the counter electrode (set to zero), also called reference electrode [1]. For thick electrolytes (e.g. of 1-2 mm thick) the half-cell potential is the electric potential drop between the current collecting grid on top of the cathode and an equipotential surface in the electrolyte bulk [1,3,23]. The rate constants in Eq. 36 can be lumped into two overall rate constants:

$$c_{f2} = K_1^t k_{f2}^0 T^{n2} \exp\left(-\frac{E_{a,f2}}{RT}\right) \tag{38}$$

$$c_{b2} = \frac{k_{f2}^t}{(K_3 K_4^t K_5)^2} \tag{39}$$

The fraction of available sites on the LSM surface $\theta_{*_{LSM_s}}$ in Eq. 36 cannot be determined. Since surface coverage tends to be a function of gas pressure and temperature [24] $\theta_{*_{LSM_s}}^2$ in Eq. 36 is replaced by an exponential dependency on the oxygen molar fraction in the gas-phase $X_{O_{2,g}}$ and on the temperature of the cell T:

$$\theta_{*_{LSM_s}}^2 = X_{O_{2,g}}^n T^m \tag{40}$$

n and m are fitting parameters of the model and are called "oxygen exponent" and "temperature exponent" respectively. With Eqs. 37 – 39 Eq. 36 can be rewritten as:

$$r_2 = c_{f2} X_{O_{2,g}} \exp\left(\frac{-(\alpha_{c2}+1)F\Delta\phi}{RT}\right) - c_{b2}\left(\frac{X_{O_{O,YSZ_b}^x}}{X_{V_{O,YSZ_b}^{\cdot\cdot}}}\right)^2 \exp\left(\frac{(\alpha_{c2}+2)F\Delta\phi}{RT}\right) \tag{41}$$

In order to reduce the number of fitting parameters Eq. 37 is rewritten as:

$$c_{f2} = A_2 \exp\left(-\frac{E_{a,f2}}{RT}\right) \tag{42}$$

where A_2 is the pre-exponential fitting parameter used in the model and is called "pre-exponent of reaction R2". The backward rate constant c_{b2} is then calculated from the Gibbs free energy change for the ORR ΔG_{ORR}:

$$O_{2,g} + 4e^- \rightleftharpoons 2O_{YSZ_b}^{2-} \tag{43}$$

$$\frac{c_{f2}}{c_{b2}} = e\mathrm{xp}\left(-\frac{\Delta G_{ORR}}{RT}\right) = \exp\left(-\frac{\Delta H_{ORR} - T\Delta S_{ORR}}{RT}\right) \tag{44}$$

The oxygen gas and the oxygen vacancy in the YSZ bulk phase are reference samples and therefore their enthalpies ($h_{O_{2,g}}$ and $h_{V_{O,YSZ_b}^{\cdot\cdot}}$) are set to zero. The enthalpy of the oxygen ion in the YSZ bulk phase h_{O_{O,YSZ_b}^x} is set to $-236\ \mathrm{kJ\ mol^{-1}}$ according to prior literature [25]. To further reduce the number of parameters the entropy change of the ORR ΔS_{ORR} is also set to zero [1]. Eq. 41 can then be rewritten as:

$$c_{b2} = c_{f2} \exp\left(-\frac{2h_{O_{O,YSZ_b}^x}}{RT}\right) \tag{45}$$

3. Results and discussion

3.1. Fitting the model to experimental data

To obtain realistic values for the pre-exponential parameter A_2, the oxygen exponent n and the temperature exponent m the experimental electrochemical impedance spectra at OCV from A. Barbucci et al. [4] are simulated. The value for the activation energy of step R2, $E_{a,f2}$, is taken from A. Banerjee and O. Deutschmann [1]. The best fitting kinetic and thermodynamic parameters are listed in Table 3. All baseline parameters for the model as well as the microstructural parameters corresponding to the symmetrical cell tested by Barbucci are given in Table 4. Figure 4 presents a comparison of the simulated electrochemical impedance spectra at OCV against Barbucci's measurements.

Table 3. Best fitting kinetic and thermodynamic parameters for the model.

Parameter	Value	Reference
Activation energy of step R2	$190\ \mathrm{kj\ mol^{-1}}$	[1]
Preexponential parameter	2.1×10^{58}	fit
Oxygen exponent	$-0.125\ \&\ -0.25$	fit
Temperature exponent	-18	fit

Table 4. Baseline model parameters and structural parameters for the experimental data from A. Barbucci et al. [4].

Parameter	Value	Reference
Cathode thickness	$43\ \mu\mathrm{m}$	[4]
Electrolyte thickness	$2000\ \mu\mathrm{m}$	[4]
Pressure	1 atm	[4]
Inlet gas velocity	$10\ \mathrm{m\ s^{-1}}$	[1]
Porosity	0.4	[1]
Porosity gradient	$0.103\ \mathrm{cm^{-1}}$	[26]
Tortuosity	2	[1]
Particle diameter	$0.3\ \mu\mathrm{m}$	[4]
LSM volume fraction	0.5	[4]
YSZ volume fraction	0.5	[4]
Gas/LSM double layer capacitance	$10\ \mu\mathrm{F\ cm^{-2}}$	[27]
LSM/YSZ double layer capacitance	$1.067 \times 10^{-6}\ \mathrm{T} - 7.438 \times 10^{-4}\ \mathrm{F\ cm^{-2}}$	[28]
LSM surface site density	$1.15 \times 10^{-9}\ \mathrm{mol\ cm^{-2}}$	[1]
YSZ surface site density	$1.25 \times 10^{-9}\ \mathrm{mol\ cm^{-2}}$	[22]

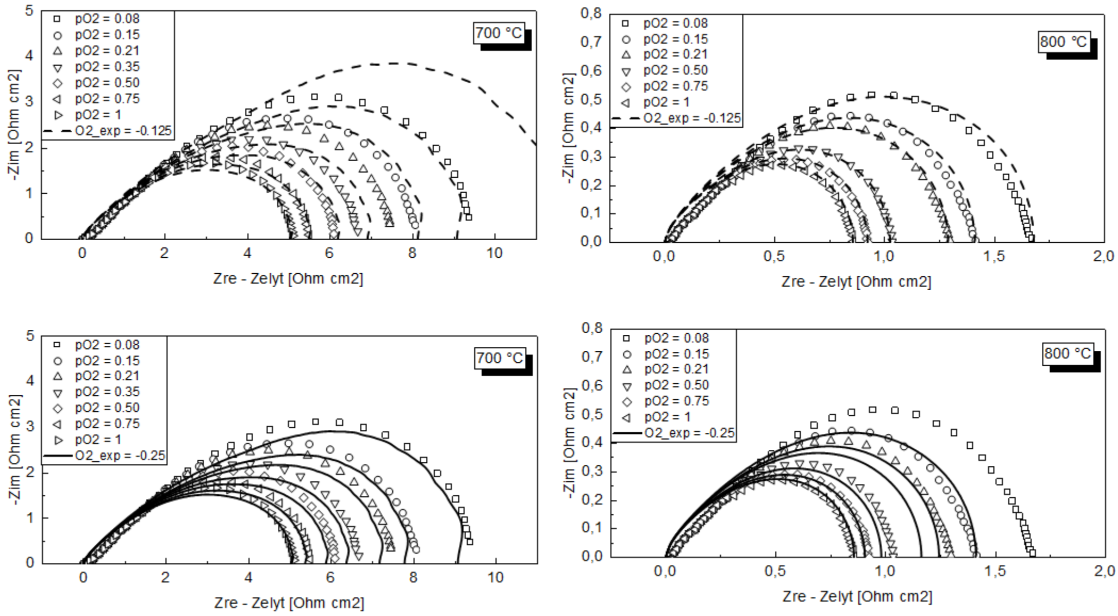

Figure 4. Nyquist plot of experimental data from A. Barbucci et al. [4] and simulated electrochemical impedance spectra over T = 973 - 1073 K at OCV and p_{O_2} = 0.08 – 1 with step R2 as RDS. Two values for the oxygen exponent n are explored (-0.125 and -0.25).

For calculation purposes, the electrolyte thickness introduced in the model doesn't always correspond to the entire thickness of the measured electrolyte. As explained in section 2.4 the potential drop across the half-cell occurs between the interface to the current collecting grid on top of the LSM-YSZ electrode and an equipotential surface in the electrolyte bulk [1,3,23]. For the thick electrode from Barbucci this equipotential surface was estimated by Banerjee and Deutschmann to lay at a distance of 350 μm from the cathode-electrolyte interphase [1]. For thin electrolytes like the ones from J.S. Cronin et al. [5], J. Nielsen and J. Hjelm. [6], and A.C. Co et al. [8] the equipotential surface lays at the electrolyte-reference electrode interface, comprising the full thickness of the electrolyte [1].

In Figure 4 the ohmic drop across the electrolyte is subtracted from the real part of the complex impedance (the horizontal axis) to focus solely on the electrode contribution. Also, all simulated spectra are multiplied by two since Barbucci's measurements were performed on a symmetrical cell where each electrode on both sides of the cell contributes equally to the spectra. The best fits are obtained with two different values for the oxygen exponent. A value of −0.125 provides an excellent fit at 800 °C for all oxygen partial pressures p_{O_2}, while at 700 °C the predicted polarization resistance R_p is larger than the experimental values, specially at lower p_{O_2}. A value of -0.25 for the oxygen exponent provides an excellent fit at 700 °C, whereas at 800 °C the R_p is smaller than experimentally measured. Since the rate of reactions decreases with decreasing temperature it is expected that kinetics contribute more to the R_p at 700 °C than at 800 °C [2]. Accounting for this the best value for the oxygen exponent is -0.25. The model is not able to deliver the correct magnitudes for the polarization resistances from Barbucci's data over both temperatures and oxygen partial pressures with a single set of kinetic parameters. The largest discrepancies are observed at lower O_2 pressures. However, the shape of the curves is very well reproduced. This is important since the shape of a EIS reflects the different molecular and physical processes occurring in the cell [1,2].

3.2. Validating the model against other data sets

With the obtained kinetic and thermodynamic parameters two additional data sets [5,6] of electrochemical impedance spectra at OCV are simulated. The structural parameters of the samples tested by J.S. Cronin et al. [5] and J. Nielsen and J. Hjelm. [7] are given in Table 5.

Table 5. Structural parameters for the experimental data from J.S. Cronin et al. [5] and J. Nielsen and J. Hjelm. [7].

Parameter	Value		Reference	
	Cronin	Nielsen	Cronin	Nielsen
Cathode thickness	10.25 μm	20 μm	[5]	[7]
Electrolyte thickness	125 μm	150 μm	[1]	[7]
Porosity	0.49	0.4	[5]	[1]
Porosity gradient	0		[1]	
Tortuosity	2.64	2	[5]	[1]
Particle diameter	0.29 μm		[1]	
LSM volume fraction	0.4765	0.5	[5]	[1]
YSZ volume fraction	0.5235	0.5	[5]	[1]
Gas/LSM specific surface area	$9.7 \times 10^4\ \mathrm{cm}^{-1}$	$1.72 \times 10^5\ \mathrm{cm}^{-1}$	[5]	[1]
LSM/YSZ specific surface area	$1.07 \times 10^5\ \mathrm{cm}^{-1}$		[5]	
LSM/YSZ double layer capacitance	$4.268 \times 10^{-6}\ \mathrm{T} - 2.975 \times 10^{-3}\ \mathrm{F\ cm}^{-2}$		[1]	
Specific three phase boundary length	$9.5 \times 10^8\ \mathrm{cm}^{-2}$		[5]	[1]

Those values which are not provided by the original authors are taken from A. Barnerjee and O. Deutschmann [1]. Cronin and coworkers provided values for the Gas/LSM and the LSM/YSZ specific surface areas as well as for the specific three phase boundary length. Therefore, these values are not calculated in this case by the model through percolation theory, as it had been done with Barbucci's data, but rather imputed directly. The value for the LSM/YSZ double layer capacitance was estimated by Barnerjee and Deutschmann and was found to provide the best results with their model. Most of the structural parameters for the data set from J. Nielsen and J. Hjelm [7]. were originally estimated by A. Barnerjee and O. Deutschmann, which introduces a great deal of uncertainty in the results, especially with the value of the Gas/LSM specific surface area, which was found to be particularly relevant for the polarization resistance [1]. Figures 5 and 6 show the simulated impedance spectra at OCV against the experimental data from J.S. Cronin et al. [5] and J. Nielsen and J. Hjelm. [7]. Also, in figures 5 and 6 the experimental measurements are corrected to remove the high frequency impedance feature due to grain boundary resistance in the YSZ phase which is not accounted for by the model [1].

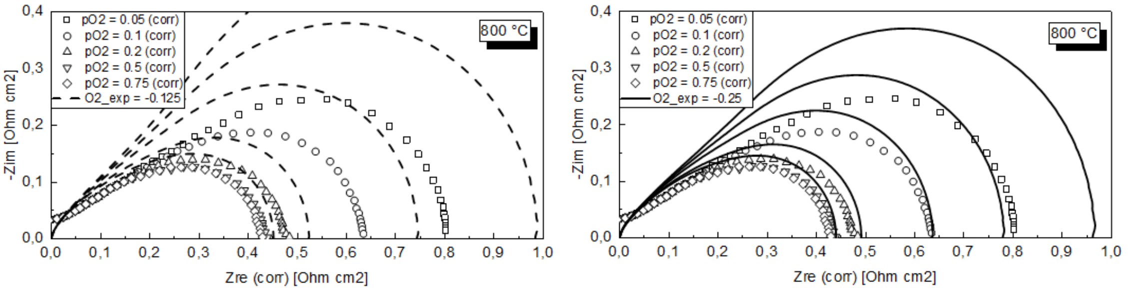

Figure 5. Nyquist plot of experimental data from J.S. Cronin et al. [5] and simulated electrochemical impedance spectra over p_{O_2} = 0.05 - 0.75 at T = 1073 K and OCV with step R2 as RDS. The experimental data is corrected to remove the high frequency impedance feature due to grain boundary resistance in the YSZ phase unaccounted for by the model. Two values for the oxygen exponent n are explored (-0.125 and -0.25).

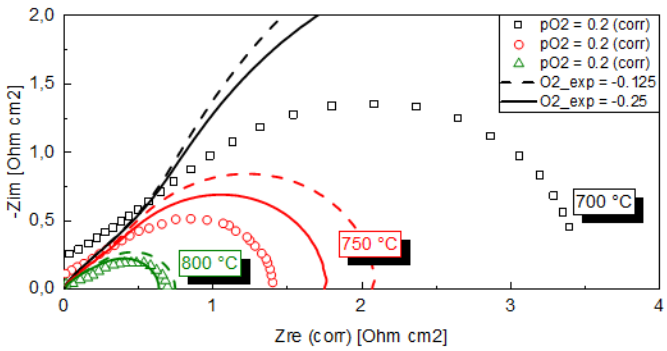

Figure 6. Nyquist plot of experimental data from J.S. Cronin et al. [5] and simulated electrochemical impedance spectra over T = 973 - 1073 K at p_{O_2} *= 0.02 and OCV with step R2 as RDS. The experimental data is corrected to remove the high frequency impedance feature due to grain boundary resistance in the YSZ phase unaccounted for by the model. Two values for the oxygen exponent n are explored (-0.125 and -0.25).*

At 800 °C the magnitudes of the polarization resistance as a function of the oxygen partial pressure in Figure 5 are not correctly reproduced. This is particularly evident in Figure 6 for lower temperatures. For lower temperatures and oxygen partial pressures the simulated R_p are too large, which indicates that the kinetics are slower than experimentally measured. However, as it is the case with Barbucci's data, the shape of the EIS curves is well captured. The only structural parameters which are not provided by J.S. Cronin et al. [5] (i.e. electrolyte thickness, porosity gradient, particle diameter, LSM/YSZ double layer capacitance) were varied to try to obtain a better agreement with the experimental measurements. However, no noticeable improvement was achieved.

Figures 6 and 7 present the simulated impedance spectra at OCV against the experimental measurements from J. Nielsen and J. Hjelm [7]. A trend like the one obtained with Cronin's data is observed. Figure 7 shows how the simulated polarization resistance at 600 °C is much larger than experimentally measured. Since the model was calibrated for temperatures between 700 °C and 800 °C greater discrepancies outside of this temperature range are more likely to occur. Figure 8 shows the simulated and the experimental impedance spectra data at 650 °C. Whereas for an p_{O_2} of 0.21 a good fit is obtained for $p_{O_2} = 1$ the simulated R_p is too large. It is important to notice, however, that the uncertainty in the simulation of Nielsen's and Hjelm's data is greater than with Cronin's data because many of the structural parameters where not measured experimentally but rather estimated by Banerjee and Deutschmann.

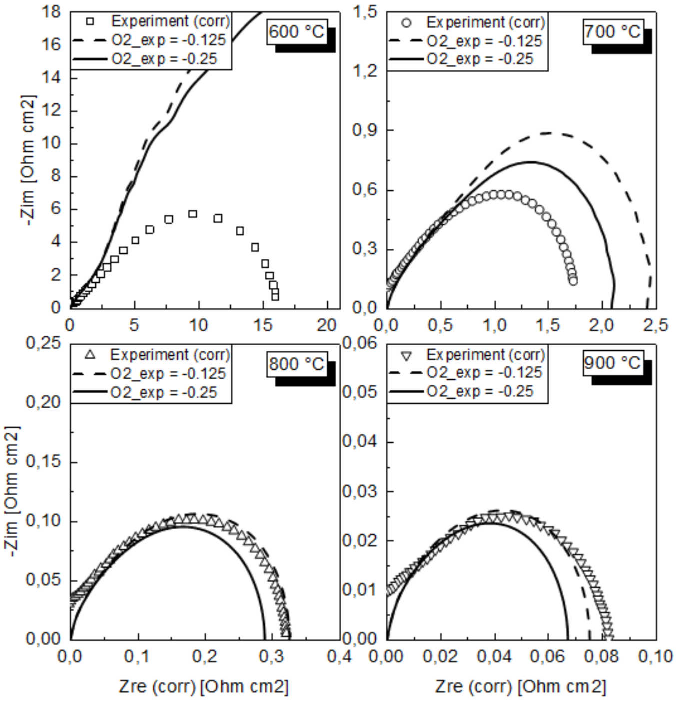

Figure 7. Nyquist plot of experimental data from J. Nielsen and J. Hjelm [7] and simulated electrochemical impedance spectra over T = 873 - 1173 K at p_{O_2} = 0.21 and OCV with step R2 as RDS. The experimental data is corrected to remove the high frequency impedance feature due to grain boundary resistance in the YSZ phase unaccounted for by the model. Two values for the oxygen exponent n are explored (-0.125 and -0.25).

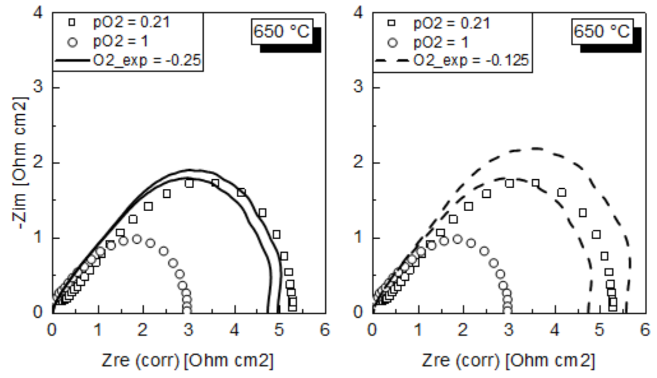

Figure 8. Nyquist plot of experimental data from J. Nielsen and J. Hjelm [7] and simulated electrochemical impedance spectra over p_{O_2} = 0.21 - 1 at T = 923 K and OCV with step R2 as RDS. The experimental data is corrected to remove the high frequency impedance feature due to grain boundary resistance in the YSZ phase unaccounted for by the model. Two values for the oxygen exponent n are explored (-0.125 and -0.25).

More relevant for studying of the performance of cells under operating conditions are measurements of the current density as a function of the polarization (also called overpotential). Figure 9 presents the simulated steady state polarization curves at multiple temperatures and over a polarization range of $-1\ \mathrm{V}$ to $+1\ \mathrm{V}$ against the experimental data from A. Barbucci et al. [4]. This measurements were performed using a three electrode configuration, in which a reference electrode (generally platinum Pt) is placed on the surface of the electrolyte pellet at some distance from the working electrode, i.e. the LSM-YSZ electrode [4]. The simulations from 700 °C to 800 °C different only slightly from the experimental data, while at 650 °C the simulated current density is too low. This could be attributed to the uncertainty in the position of the equipotential surface in the electrolyte bulk. Also, the three electrode configuration used by Barbucci could have contributed to this discrepancy [1], since it is known that the inherent asymmetry introduced by the presence of a reference electrode can create a significant distortion of the measurements [2].

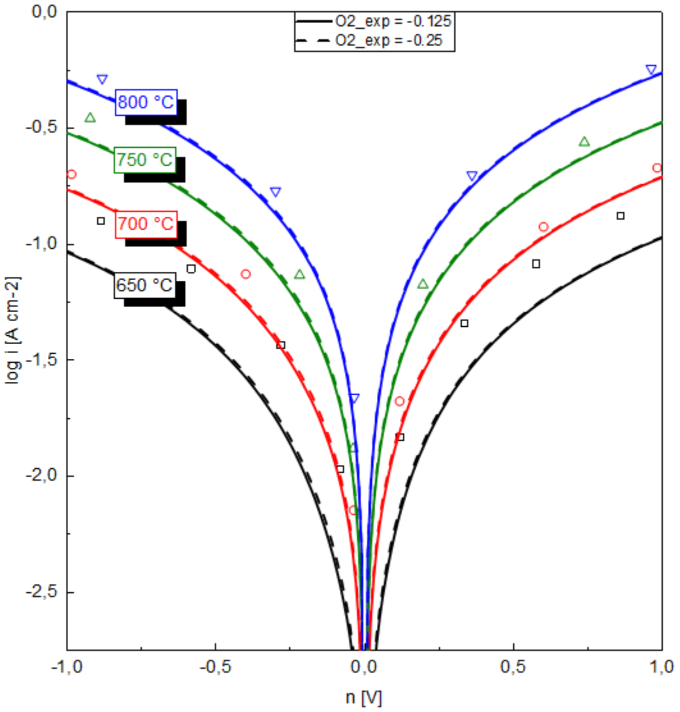

Figure 9. Steady state polarization curves of experimental data from A. Barbucci et al. [4] and simulation over an overpotential range of -1 V to +1 V over T = 923 - 1073 K at p_{O_2} = 0.2095 with step R2 as RDS. Two values for the oxygen exponent n are explored (-0.125 and -0.25).

The model is also validated against experimental data from A.C. Co et al. [8], J. Soderberg et al. [9], Y.J Leng et al. [11], and K. Hayashi et al. [10]. The structural parameters for these data sets are provided in Tables 6 and 7. Figure 10 to 13 show the simulated steady state polarization curves against the experimental measurements for all data sets.

Table 6. Structural parameters for the experimental data from A.C. Co et al [8] and J.N. Soderberg et al. [9].

Parameter	Value		Reference	
	Co	Soderberg	Co	Soderberg
Cathode thickness	30 μm	10 μm	[8]	[9]
Electrolyte thickness	200 μm	1000 μm	[8]	[9]
Porosity	0.4	0.1725	[1]	[9]
Porosity gradient	0		[1]	
Tortuosity	2		[1]	
Particle diameter	0.2 μm	0.2 μm	[8]	[9]
LSM volume fraction	0.5	0.5	[8]	[9]
YSZ volume fraction	0.5	0.5	[8]	[9]

Table 7. Structural parameters for the experimental data from Y.J. Leng, et al. [11] and K. Hayashi et al. [10].

Parameter	Value		Reference	
	Leng	Hayashi	Leng	Hayashi
Cathode thickness	10 μm	560 μm	[11]	[10]
Electrolyte thickness	750 μm	1000 μm	[11]	[10]
Porosity	0.4		[1]	
Porosity gradient	0		[1]	
Tortuosity	2		[1]	
Particle diameter	0.3 μm	40 nm	[11]	[10]
LSM volume fraction	0.5	0.5	[11]	[10]
YSZ volume fraction	0.5	0.5	[11]	[10]

For A.C. Co et al. the value of the electrolyte thickness introduced in the model corresponds to the full thickness of the electrolyte. For Soderberg, Leng and Hayashi this value was varied to achieve a better agreement between simulation and experiment.

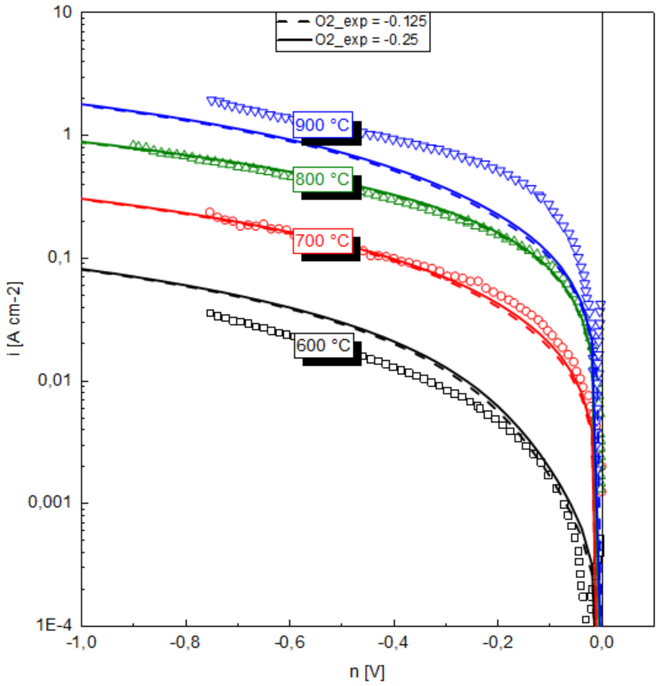

Figure 10. Steady state polarization curves of experimental data from A.C. Co et al. [8] *and simulation over an overpotential range of -1 V to 0 V over T = 873 - 1173 K at* p_{O_2} *= 0.2095 with step R2 as RDS. Two values for the oxygen exponent n are explored (-0.125 and -0.25).*

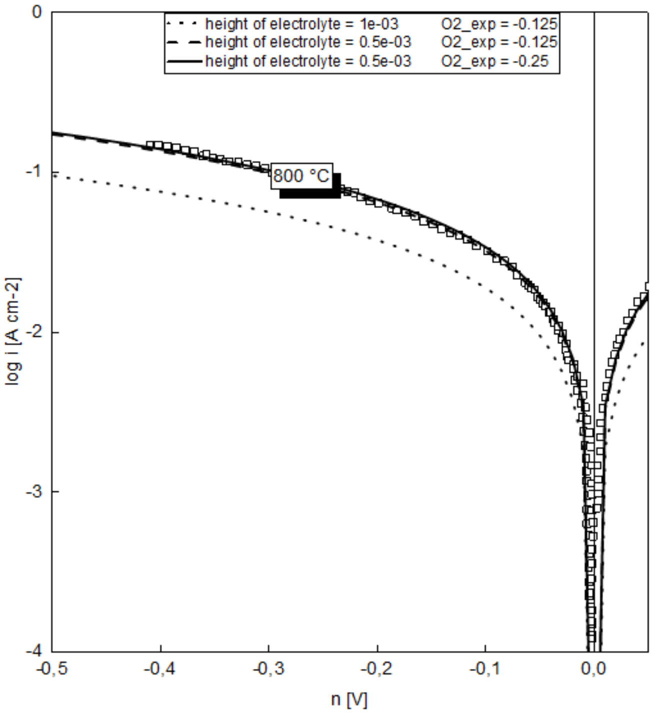

Figure 11. Steady state polarization curves of experimental data from J.N. Soderberg et al. [9] *and simulation over an overpotential range of -1 V to 0 V at T = 1073 K and* p_{O_2} *= 0.2095 with step R2 as RDS. Two values for the oxygen exponent n are explored (-0.125 and -0.25).*

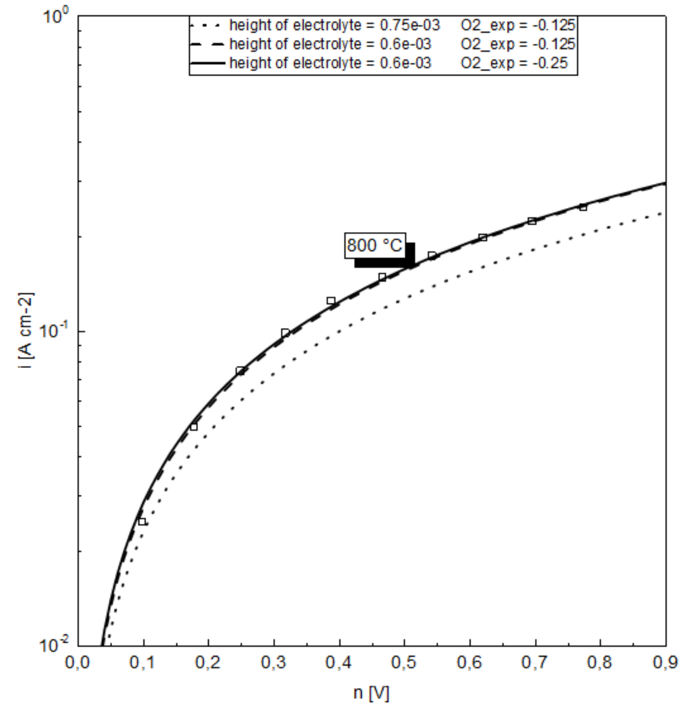

Figure 12. Steady state polarization curves of experimental data from Y.J. Leng, et al. [11] and simulation over an overpotential range of 0 V to +0.9V at T = 1073 K and p_{O_2} = 0.2095 with step R2 as RDS. Two values for the oxygen exponent n are explored (-0.125 and -0.25).

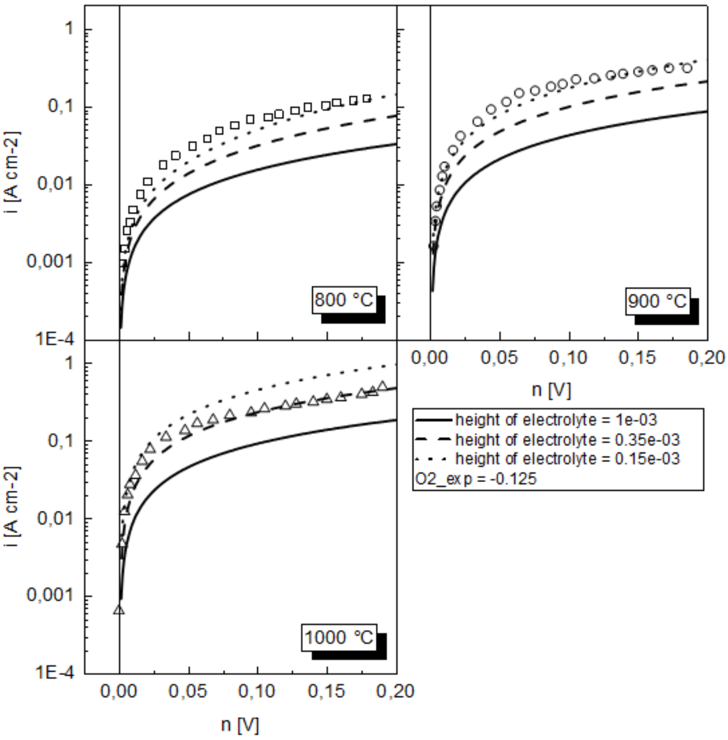

Figure 13. Steady state polarization curves of experimental data from K. Hayashi et al. [10] and simulation over an overpotential range of 0 V to +0.2 V over T = 1073 - 1273 K and p_{O_2} = 0.2095 with step R2 as RDS.

In Figure 10 an excellent agreement between simulation and experiment is obtained for 700 °C and 800 °C. For 600 °C and 900 °C, which lay outside the temperature range in which the model was calibrated, the discrepancies are large in terms of the magnitude of the current density and the shape of the curve. At 900 °C the curve becomes slightly steeper for overpotentials above −0.5. This could be attributed to the spillover of oxygen ions $\mathrm{O}^{-}_{\mathrm{LSM_s}}$ across the three phase boundary (step R4) becoming co-limiting, which is known to occur at higher overpotentials [1]. Figures 11 and 12 show the impact of the position of the electrolyte bulk equipotential surface on the current density. By setting the electrolyte thickness in the model to 500 µm and 600 µm for Soderberg and Leng respectively, an excellent agreement between simulation and experiment is achieved. For the data set from Hayashi, shown in Figure 13, the shape of the curve is best captured by setting the electrolyte thickness in the model to 350 µm, whereas the magnitude of the current density at 800 °C and 900 °C is best simulated with an electrolyte thickness of 150 µm. At 1000°C the discrepancy between simulation and experiment is more evident. In Figures 9 to 13 the difference between simulations ran with an oxygen exponent of −0.125 and −0.25 is negligible.

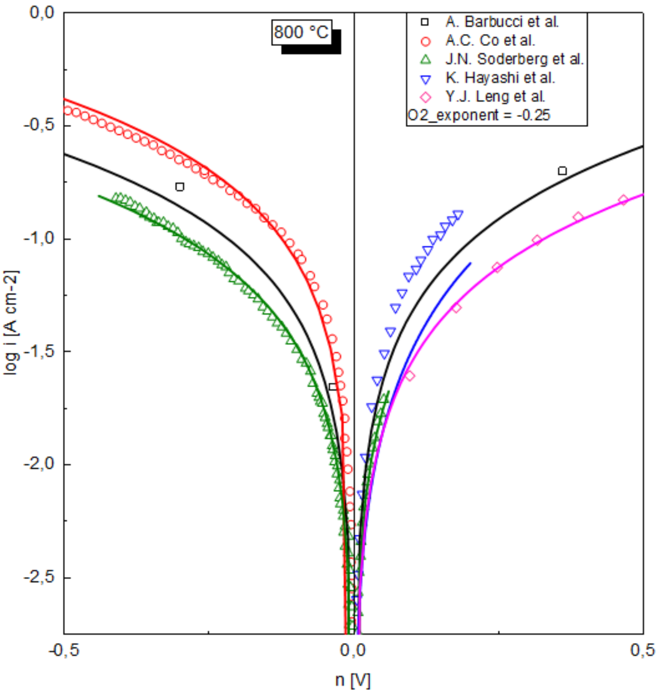

Figure 14. Steady-state polarization curves for experimental data from A. Barbucci et al., [4] A.C. Co et al., [8] J.N. Soderberg et al., [9] Y.J. Leng, et al., [11] and K. Hayashi et al. [10] and simulation over an overpotential range of -0.5 V to +0.5 V at p_{O_2} = 0.2095 atm and T = 923 K with step R2 as RDS.

Figure 14 depicts the importance of the microstructure of the cathode for the cell performance by presenting a comparison of simulation and experiment for all data sets at 800 °C in air (p_{O_2} = 0.2095) over an overpotential range of -0.5 V to $+0.5$ V. Here it can be seen how cells with different structural characteristics behave differently, even though they consist of the same materials: a composite LSM-YSZ cathode sintered on a dense YSZ electrolyte. Furthermore Figure 14 shows how the model responds to changes in the microstructure. If this wouldn't be the case, all simulations would fall together.

4. Conclusion and outlook

The reduced kinetic model presented in sections 2.1 and 2.2 of this work, including the kinetic and thermodynamic parameters summarized in Table 3, can reproduce electrochemical impedance spectra (EIS) and steady state polarization curves measured on LSM-YSZ composite cathodes sintered on dense YSZ electrolytes with different microstructures and under multiple conditions with a certain degree of discrepancy. EIS curves proved to be particularly difficult to simulate with the present model. Better results were obtained by simulating the dependency of the current density on the polarization. However, the large discrepancies obtained by simulating at temperatures outside the original temperature range in which the model was calibrated are strong indicators that the model is not fully intrinsic. Moreover, the lack of microstructural information increases the number of parameters that must be estimated, which also increases the uncertainty of the simulations.

The model presented in this work should continue to be improved. A better fit of the experimental data sets at OCV used in this work should be attempted by modifying the estimated microstructural parameters. Modifications of the reduced kinetic model might as well be necessary. Furthermore, experimental measurements performed on microstructurally well characterized samples are required, i.e. with known cathode and electrolyte thickness, as well as porosity, porosity gradient, tortuosity, particle diameter, volume fraction of LSM and YSZ, Gas/LSM specific surface area, LSM/YSZ specific surface area, LSM/YSZ double layer capacitance, and specific three phase boundary length. It is also recommendable to consider the spillover of $\mathrm{O}^{-}_{\mathrm{LSM}_\mathrm{s}}$ oxygen ions across the three-phase boundary (step R4) as a co-limiting reaction step at higher polarizations. To be able to find the appropriate kinetic and thermodynamic parameters for this reaction electrochemical impedance spectra measured under polarization would be required. The contribution of steps R2 and R4 to the polarization resistance and the current density should then be set as a function of the polarization.

5. References

[1] A. Banerjee, O. Deutschmann, *J. Catal.* **2017**, *346*, 30–49.

[2] S. B. Adler, *Chem. Rev.* **2004**, *104*, 4791–4844.

[3] W. G. Bessler, S. Gewies, M. Vogler, *Electrochimica Acta* **2007**, *53*, 1782–1800.

[4] A. Barbucci, M. Paola Carpanese, M. Viviani, N. Vatistas, C. Nicolella, *J. Appl. Electrochem.* **2009**, *39*, 513–521.

[5] J. S. Cronin, K. Muangnapoh, Z. Patterson, K. J. Yakal-Kremski, V. P. Dravid, S. A. Barnett, *J. Electrochem. Soc.* **2012**, *159*, B385–B393.

[6] J. Nielsen, J. Hjelm, *Electrochimica Acta* **2014**, *115*, 31–45.

[7] J. Nielsen, J. Hjelm, *Electrochimica Acta* **2014**, *115*, 31–45.

[8] A. C. Co, S. J. Xia, V. I. Birss, *J. Electrochem. Soc.* **2005**, *152*, A570.

[9] J. N. Soderberg, L. Sun, P. Sarkar, V. I. Birss, *J. Electrochem. Soc.* **2009**, *156*, B721.

[10] K. Hayashi, M. Hosokawa, T. Yoshida, Y. Ohya, Y. Takahashi, O. Yamamoto, H. Minoura, *Mater. Sci. Eng. B* **1997**, *49*, 239–242.

[11] Y. J. Leng, S. H. Chan, K. A. Khor, S. P. Jiang, *J. Appl. Electrochem.* **2004**, *34*, 409–415.

[12] H. Zhu, R. J. Kee, V. M. Janardhanan, O. Deutschmann, D. G. Goodwin, *J. Electrochem. Soc.* **2005**, *152*, A2427.

[13] V. M. Janardhanan, O. Deutschmann, *Chem. Eng. Sci.* **2007**, *62*, 5473–5486.

[14] H. D. Baehr, K. Stephan, *Wärme- und Stoffübertragung*, Springer Berlin Heidelberg, Berlin, Heidelberg, **2016**.

[15] J. Bear, *Dynamics of Fluids in Porous Media*, Dover, New York, **1988**.

[16] V. M. Janardhanan, O. Deutschmann, *Electrochimica Acta* **2011**, *56*, 9775–9782.

[17] J. G. Pharoah, K. Karan, W. Sun, *J. Power Sources* **2006**, *161*, 214–224.

[18] W. Kiatkittipong, T. Tagawa, S. Goto, S. Assabumrungrat, P. Praserthdam, *Chem. Eng. J.* **2005**, *106*, 35–42.

[19] J. R. Ferguson, J. M. Fiard, R. Herbin, *J. Power Sources* **1996**, *58*, 109–122.

[20] A. Bertei, C. Nicolella, *Powder Technol.* **2011**, *213*, 100–108.

[21] O. Deutschmann, Ed. , *Modeling and Simulation of Heterogeneous Catalytic Reactions: From the Molecular Process to the Technical System*, Wiley-VCH, Weinheim, **2012**.

[22] D. G. Goodwin, H. Zhu, A. M. Colclasure, R. J. Kee, *J. Electrochem. Soc.* **2009**, *156*, B1004.

[23] S. B. Adler, *J. Electrochem. Soc.* **2002**, *149*, E166–E172.

[24] I. Chorkendorff, J. W. Niemantsverdriet, *Concepts of Modern Catalysis and Kinetics*, Wiley-VCH, Weinheim, Germany, **2017**.

[25] M. Vogler, A. Bieberle-Hütter, L. Gauckler, J. Warnatz, W. G. Bessler, *J. Electrochem. Soc.* **2009**, *156*, B663.

[26] A. Bertei, A. Barbucci, M. P. Carpanese, M. Viviani, C. Nicolella, *Chem. Eng. J.* **2012**, *207–208*, 167–174.

[27] J. Fleig, *Phys Chem Chem Phys* **2005**, *7*, 2027–2037.

[28] M. Hendriks, J. E. Ten Elshof, H. J. M. Bouwmeester, H. Verweij, *Solid State Ion.* **2002**, *146*, 211–217.

Acknowledgements

I would like to hereby thank Prof. Dr. Olaf Deutschmann for the opportunity to do the present thesis under the chair of Chemical Technology of the Institute for Chemical Technology and Polymer Chemistry at the Karlsruhe Institute of Technology.

I would also particularly like to thank Mr. Aayan Banerjee for his continuous professional support and knowledge which made this thesis possible.

Erklärung

Ich versichere wahrheitsgemäß, die Arbeit selbstständig verfasst, alle benutzten Hilfsmittel vollständig und genau angegeben und alles kenntlich gemacht zu haben, was aus Arbeiten Anderer unverändert oder mit Abänderungen entnommen wurde sowie die Satzung des KIT zur Sicherung guter wissenschaftlicher Praxis in der jeweils gültigen Fassung beachtet zu haben.

Darüber hinaus versichere ich, dass die in der Arbeit verwendeten Ergebnisse in dem vom Prüfungsausschuss festgelegten Zeitraum der Arbeit entstanden sind.“

Karlsruhe, den

Aaron Useche Esclasans